ELSEVIER

Earth and Planetary Science Letters 203 (2002) 131–148

EPSL

www.elsevier.com/locate/epsl

Mechanisms of magmatic gas loss along the Southeast Indian Ridge and the Amsterdam –St. Paul Plateau

P.G. Burnard [a,*], D.W. Graham [b], K.A. Farley [a, b]

[a] *Division of Geological and Planetary Sciences, California Institute of Technology, MS100-23 Pasadena, CA 91125, USA*
[b] *College of Oceanic and Atmospheric Sciences, Oregon State University, Corvallis, OR 97331-5503, USA*

Received 20 November 2001; received in revised form 10 April 2002; accepted 12 July 2002

Abstract

New analyses of He, Ne, Ar and CO_2 trapped in basaltic glasses from the Southeast Indian Ridge (Amsterdam–St. Paul (ASP) region) show that ridge magmas degas by a Rayleigh distillation process. As a result, the absolute and relative noble gas abundances are highly fractionated with $^4He/^{40}Ar^*$ ratios as high as 620 compared to a production ratio of ~ 3 (where $^{40}Ar^*$ is ^{40}Ar corrected for atmospheric contamination). There is a good correlation between $^4He/^{40}Ar^*$ and the MgO content of the basalt, suggesting that the amount of gas lost from a particular magma is related to the degree of crystallization. Fractional crystallization forces oversaturation of CO_2 because CO_2 is an incompatible element. Therefore, crystallization will increase the fraction of gas lost from the magma. The He–Ar–CO_2–MgO–TiO_2 compositions of the ASP basalts are modeled as a combined fractional crystallization–fractional degassing process using experimentally determined noble gas and CO_2 solubilities and partition coefficients at reasonable magmatic pressures (2–4 kbar). The combined fractional crystallization–degassing model reproduces the basalt compositions well, although it is not possible to rule out depth of eruption as a potential additional control on the extent of degassing. The extent of degassing determines the relative noble gas abundances ($^4He/^{40}Ar^*$) and the $^{40}Ar^*/CO_2$ ratio but it cannot account for large ($>$ factor 50) variations in He/CO_2, due to the similar solubilities of He and CO_2 in basaltic magmas. Instead, variations in $CO_2/^3He$ ($\equiv C/^3He$) trapped in the vesicles must reflect similar variations in the primary magma. The controls on $C/^3He$ in mid-ocean ridge basalts (MORBs) are not known. There are no obvious correlated variations between $C/^3He$ and tracers of mantle heterogeneity ($^3He/^4He$, K/Ti etc.), implying that the variations in $C/^3He$ are not likely to be a feature of the mantle source to these basalts. Mixing between MORB-like sources and more enriched, high $^3He/^4He$ sources occurs on and near the ASP plateau, resulting in variable $^3He/^4He$ and K/Ti compositions (and many other tracers). Using $^4He/^{40}Ar^*$ to track degassing, we demonstrate that mixing systematics involving He isotopes are determined in large part by the extent of degassing. Relatively undegassed lavas (with low $^4He/^{40}Ar^*$) are characterized by steep $^3He/^4He$–K/Ti mixing curves, with high He/Ti ratios in the enriched magma (relative to He/Ti in the MORB magma). Degassed samples (high $^4He/^{40}Ar^*$) on the other hand have roughly equal He/Ti ratios in both end-members, resulting in linear mixing trajectories involving He isotopes. Some degassing of ASP magmas must occur at depth, prior to magma mixing. As a result of degassing prior to mixing, mixing systematics of oceanic basalts that involve noble gas–lithophile pairs (e.g. $^3He/^4He$ vs. $^{87}Sr/^{86}Sr$ or $^{40}Ar/^{36}Ar$ vs. $^{206}Pb/^{204}Pb$) are unlikely to reflect the noble gas composition of the mantle source to the basalts. Instead, the mixing curve will reflect the extent of gas loss from the magmas, which is in turn buffered by the pressure

* Corresponding author. Present address: Department of Earth and Space Sciences, P.O. Box 951567, University of California at Los Angeles, Los Angeles, CA 90095-1567, USA..

PII: S0012-821X(02)00828-2

of combined crystallization–degassing and the initial CO_2 content.

Keywords: Southeast Indian Ridge; degassing; magmas; noble gases; fractional crystallization

1. Introduction

Noble gases provide key evidence of the origin and age of geochemical heterogeneities in the Earth's mantle. The fact that ^{3}He, which is not recycled or produced in significant quantities over time in the mantle, is present in mantle-derived fluids and rocks is proof that the Earth is still outgassing volatiles that have been trapped within the Earth for 4.5 Ga [1,2]. Furthermore, differences in the ratio of primordial:radiogenic (or nucleogenic) noble gas isotopes between mid-ocean ridge basalts (MORBs) and ocean island basalts (OIBs) reveal that there have been time-integrated variations in noble gas/(U, Th or K) of their mantle sources. Previous work has shown that helium in the mantle source of MORBs is more radiogenic and neon is more nucleogenic than the He and Ne typically found in OIB source regions. The trace element-depleted MORB source region has had lower time-integrated ^{3}He/U+Th and ^{22}Ne/U+Th ratios than the 'enriched' OIB source region ([3] and references therein). Concentrations of U in most OIB sources are unlikely to be lower than in the MORB source [4], therefore it seems inescapable that the mantle source of most OIB volcanism has higher concentrations of the primordial noble gas isotopes (e.g. ^{22}Ne and ^{3}He) than the mantle source of MORBs.

The isotope compositions of noble gases – particularly those of He – are well defined in mantle materials and, as a result, provide important constraints on models of mantle evolution. However, noble gases are readily fractionated from each other during magmatic processes. As a consequence, the absolute and relative abundances of noble gas in the mantle are subject to considerable uncertainty. Fractionation occurs because CO_2 is relatively insoluble in silicate melts and will exolve to form a two-phase magma (melt+CO_2-dominated gas) at pressures up to 10 kbar depending on the initial CO_2 content of the magma [5]. In the presence of a volatile phase, noble gases partition between vesicles and melt depending on their solubilities. Helium is about 10 times more soluble than Ar in basaltic melts [6–8], and therefore the He/Ar ratio of the bubbles will be a maximum of 10 times lower than that of the parent liquid. Any bubble loss (degassing) will result in an increase in the He/Ar ratio of the residual melt. The ^{4}He/^{40}Ar* ratio (where ^{40}Ar* is the ^{40}Ar corrected for atmospheric contribution by assuming that all ^{36}Ar is derived from the atmosphere) provides a useful index for tracking degassing of a magma, as the initial ^{4}He/^{40}Ar* must lie between 2 and 4 given the known range in U+Th/K of the mantle [9,10]. Relative noble gas abundances in basalts are therefore excellent tracers of magmatic gas processes. In this contribution, we use relative noble gas abundances to trace the relationship between volatile and lithophile tracers in a suite of basalts from the Amsterdam–St. Paul Plateau on the Southeast Indian Ridge.

1.1. Amsterdam–St. Paul: previous work

The majority of fluids and basalts produced at mid-ocean ridges have a near-constant ^{3}He/^{4}He ratio of $\approx 8 \pm 1.5$ Ra, where Ra is the atmospheric ^{3}He/^{4}He ratio $= 1.39 \times 10^{-6}$ [11]. However, some sections of mid-ocean ridge sample a region of mantle with higher ^{3}He/^{4}He ratios, typically 14–16 Ra [12–15]. These sections of mid-ocean ridge commonly form topographic highs that are geochemically distinct from 'normal' ridge segments to either side.

One such ridge-centered anomaly is the Amsterdam–St. Paul (ASP) Plateau on the Southeast Indian Ridge (SEIR)(see [16] for a location map), where there is a marked increase in ^{3}He/^{4}He on the plateau relative to 'normal' ridge segments to its northwest and southeast [16]. This is accompanied by 'enriched' geochemical patterns such as

high K/Ti and more radiogenic Sr and Pb isotopic compositions [16–18].

While the high $^3He/^4He$ peak coincides (geographically) with the occurrence of high K/Ti basalts, the relationship between He isotopes and basalt geochemistry is not straightforward. If the range in $^3He/^4He$ and K/Ti was generated by mixing of two sources (one low $^3He/^4He$, low K/Ti, the other high $^3He/^4He$, high K/Ti) with constant He and Ti concentrations, then a single mixing line in $^3He/^4He$ vs. K/Ti space is expected [19]. However, the compositions of the ASP Plateau basalts do not lie on a single line in a plot of $^3He/^4He$ vs. K/Ti (figure 3 in [16]), rather, they define a broad area with a rough positive correlation. The $^3He/^4He$–K/Ti relationships are consistent with the $(He/Ti)_{EM}/(He/Ti)_{DM}$ varying between ≈ 0.5 and ≈ 50 [16] (subscripts EM and DM correspond to 'Enriched Mantle' and 'Depleted Mantle' sources respectively). Because the measured He contents of basalt glasses are unreliable indicators of the He concentration of the parent magma due to heterogeneous distribution of vesicles in the glass and/or due to late stage degassing during eruption of the lava, mixing systematics involving isotope and/or trace element ratios are a preferable method for probing relative He abundances.

These large variations in He content are most plausibly related to either the way that volatiles are extracted from the mantle during melting, with previous (deeper) episodes of melting depleting or 'mining' He from some sections of mantle [16], or to some gas loss from the magma(s) prior to mixing. We present He, Ne, Ar and CO_2 data on the same suite of basaltic glasses that were analyzed by [16] in order to fully examine the history of volatile loss along this section of the SEIR, and to demonstrate the potential of using relative noble gas abundances for tracking magmatic degassing.

2. Analytical technique

Glassy rinds of pillow basalts were gently broken up using a small chisel into the largest possible fragments that would fit into the crushing apparatus, about 5–8 mm diameter. The cleanest pieces with the highest proportion of glass were selected, although inevitably some of these large pieces contained small feldspar phenocrysts and/or minor reddish brown alteration; where this occurred, it has been noted in Table 1. Between 4 and 6 chunks were cleaned (ultrasonic cleaning in diluted HNO_3 followed by several washes with water and ethanol), then loaded into online crushing devices essentially the same as those described by [20]. The samples were baked under ultra-high vacuum for ca. 6 h at 120°C, then pumped at room temperature for a further 18 h to reduce surficial contaminants.

The samples were analyzed by sequential crushing using an all-metal extraction system. Crushing releases volatiles trapped in vesicles as opposed to the glassy matrix. Sequential crushing will liberate gases from progressively smaller vesicles as crushing proceeds. Small vesicles grow during magmatic ascent due to decompression, thus the largest vesicles formed first in the magmatic history and contain the earliest volatiles [21]. Sequential crushing, by analyzing differently sized vesicles, allows the vesicle 'chronology' to be interrogated. Each sample was incrementally crushed in three to nine steps, with the gases extracted and measured at each step. The first crushing step of each analysis was extremely gentle, designed to release as little gas from the sample as possible, but to maximize release of any remaining surficial gases. Either the largest vesicles have the highest proportion of atmospheric gases or the procedure was effective at reducing atmospheric contamination in later crushes as the ratio of magmatic (e.g. ^3He) to atmospheric gases (e.g. ^{36}Ar) increases as crushing progressed (Tables 2 and 3). The second and third crushing steps (or, in some gas-rich samples such as WC49 and D47-6, the fourth step as well) released the majority of gas from the sample. The final crush of each sample released whatever gas remained in the sample.

The isotopes and abundances of He and Ne were measured on a MAP 215-50 noble gas mass spectrometer and Ar on a modified Nuclide 12 cm, 90° instrument. The gases were purified using two SAES NP10 Zr–Al getters (one at 450°C, the other at room temperature), then

Table 1
Sample locations and weights

Sample	Crush no.	Weight (g)	Efficiency[a] (%)	Segment[b]	Depth (m)	Latitude (°S)	Longitude (°E)	Distance[c] (km)	Comments
D76-2	Total	0.693	29	F	2178	−32.76	77.89	−447	
D77-2	Total	0.553	32	F	2835	−32.95	77.82	−437	minor plag
D75-1	Total	0.860	22	ZFZ	3269	−35.28	78.60	−205	
WC49	Total	0.564	23	H	3086	−35.64	78.46	−186	
WC47	Total	0.840	17	H	2840	−35.94	78.71	−146	
D73-3	Total	0.670	18	H	2659	−36.07	78.83	−129	
D73-4	Total	0.847	16	H	2659	−36.07	78.83	−129	plag
D73-5	Total	0.915	19	H	2659	−36.07	78.83	−129	plag
WC46	Total	0.733	21	H	2734	−36.18	78.95	−112	minor plag
D71-3	Total	0.832	25	I1	1940	−37.06	78.24	−89	plag
D71-1	Total	0.927	16	I1	1940	−37.06	78.24	−89	minor plag
D64-3	Total	1.043	14	I2	1805	−37.98	78.16	−21	
D63-1	Total	0.940	19	I2	1838	−38.20	78.37	9	brown alteration
D60-1	Total	0.778	18	J1	1978	−38.96	78.11	54	minor plag
D47-6	Total	0.721	23	J3	2845	−40.55	78.14	184	minor plag
D43-2	Total	0.685	5	J4	2785	−41.25	79.11	296	
D39-1	Total	0.636	19	K	2776	−41.24	81.15	416	minor plag
D34-1	Total	0.799	28	L	2480	−41.52	87.09	807	
D33-1	Total	0.777	25	L	2450	−42.12	88.04	910	minor plag

[a] 'Efficiency' is a measure of the crushing efficiency, determined by the fraction of sample that passes through a 104 μm sieve.
[b] Segments are given in [16].
[c] 'Distance' is the distance from St. Paul Island through the rotation pole of the plate (13.2°N, 38.2°E).

sorbed onto charcoal for cryogenic separation. Prior to gas purification, the amount of gas released by crushing was measured as a pressure change on a Baratron 222B 1-Torr capacitance manometer. Previous experience has shown that the pressure rise when crushing basaltic glass is due to gases that are dominantly (>90% [22,23]) CO_2. Helium, Ne and Ar were sequentially desorbed off the charcoal, then individually admitted into the relevant mass spectrometer. The pressure in the extraction line was monitored using the capacitance manometer as crushing progressed, allowing excellent control on the amount of gas released during each crushing step. The sample was not crushed to a complete powder as CO_2 is adsorbed on the crushed powder [24]; the likely effects of CO_2 adsorption on measured noble gas/CO_2 ratios is discussed in [27]. Independent experiments at Caltech show that adsorbed CO_2 is not reversibly released by heating the powder to 120°C (unpublished data).

Abundances of the noble gases were determined by peak-height comparison (^{4}He and ^{40}Ar on a Faraday cup, the remaining isotopes on a Galileo 4869 Channeltron in pulse counting mode) with standard pipettes from a tank of reduced pressure air that had been modified by adding He. The 'air' pipette has a ^{3}He/^{4}He ratio of 2.04 Ra and ^{4}He/^{40}Ar ratio of 1.42; all other isotopes and abundances are air-like, and each pipette delivers 0.1 μcc STP ^{40}Ar. Non-linearities in the response of the mass spectrometer [25] were addressed by running multiple standards in the same size range as the samples (14.3–498 ncc STP ^{4}He and 10.8–361 ncc STP ^{40}Ar). To ensure that He measurements were performed with similar amounts of He in the mass spectrometer as the calibrations – despite a large range in He/Ar in the samples – an accurately calibrated volume allowed either 77% or 93% of the He to be discarded after separation from Ne. Isobaric interferences with ^{20}Ne and ^{22}Ne (by $^{40}Ar^{2+}$ and $^{12}C^{16}O_2^{2+}$, respectively)

were corrected by independently determining the $^{40}Ar^{2+}/^{40}Ar^{+}$ and CO_2^{2+}/CO_2^{+} ratios; these were typically $<25\%$ and 1.3–1.5%, respectively. Corrections at $m/z=20$ were usually negligible ($\ll 1\%$ due to a liquid nitrogen trap close to the ion source that maintained low Ar pressures in the mass spectrometer), but relatively high CO_2 backgrounds in the mass spectrometer meant that significant corrections had to be made at $m/z=22$. Analyses where the correction exceeded 20% of the $m/z=22$ signal are not considered reliable and have not been quoted. Virtually all the error in $^{20}Ne/^{22}Ne$ and $^{21}Ne/^{22}Ne$ ratios results from these large corrections. Note that the quoted errors combine the reproducibility of at least 10 air pipettes with the within-run counting statistics. This procedure may overestimate measurement uncertainties because errors can be counted twice. However, in practice, the within-run statistical errors are usually trivial relative to the reproducibility of the air pipettes.

After analysis, each sample was unloaded from the UHV crusher and sieved to determine the crushing efficiency. Typically, only 15–30% of the crushed sample would pass through a 104 μm sieve (Table 1). Increasing the number of crushing strokes increased the fraction of sample that passed through a 100 μm sieve by creating powder out of the ca. 100 μm glass; larger fragments (1–2 mm) were not significantly crushed by increasing the number of crushing strokes because the large fragments become supported by powder. Therefore further crushing was generally not worthwhile because:

1. Further crushing released little or no additional noble gases, suggesting that the noble gases are trapped in vesicles >100 μm;
2. as grain sizes decreased, He is released by diffusion from the glass (experiments showed that up to 10 ncc STP ^{4}He was released per hour from the crush residue);
3. CO_2 is adsorbed on the glass powder remaining in the crushing apparatus.

As a result, completely powdering the sample results in He–Ar–CO_2 measurements that are not representative of the gases trapped in the vesicles.

3. Results

Twenty basalt glasses from the SEIR between 77°16′E and 88°04′E were crushed in a total of 95 individual crushing steps, usually three or four steps per sample. The He, Ne, Ar, and the CO_2 abundances are reported in Table 2, and the isotopic compositions of He, Ne and Ar are reported in Table 3. Blank contributions were insignificant ($^{40}Ar \leq 0.4\times10^{-9}$ cm^3 STP; $^{20}Ne \leq 2\times10^{-12}$ cm^3 STP; ^{4}He was below detection, $<1\%$ of the total gas released from any sample), except for Ne. Neon blanks in some cases were $\approx 5\%$ of the total Ne released from the sample, but, because blanks are air-like, blank-correcting the data does not improve precision, it merely moves the analysis along a well defined mixing line between air and the measured ratio, therefore Ne measurements were not corrected for blank contribution. The Ar blank was not air-like ($^{40}Ar/^{36}Ar \approx 200$ due to non-resolvable hydrocarbon species at m/z, allowing a direct comparison of sample heterogeneity and inter-laboratory accuracy.

3.1. Helium

Helium isotopic compositions generally agree within 5% between the two laboratories, similar to the analytical uncertainties quoted for the Caltech lab; note that the Caltech protocol was not optimized for high precision He isotope analysis as precise He isotope ratios had already been measured on this sample suite [16]. The $^3He/^4He$ ratios of two samples, WC46 and WC47, do not agree within the estimated analytical errors; in both instances, the Caltech lab $^3He/^4He$ ratios are higher by 2 Ra compared with those measured by [16]. Note that these two samples are from segments that have variable $^3He/^4He$ ratios. In addition, there are two different rock types recovered in WC47 [26]. Further analyses are planned to investigate if this discrepancy is related to analytical artifacts or reflects sample heterogeneity.

Helium abundances do not agree well between datasets, with the Caltech lab reporting 30% lower He abundances relative to the [16] study, with a lot of scatter. This systematic difference between

datasets is likely due to the different extraction techniques: typically only 20–30% of the sample was crushed to <100 μm grain size at Caltech (Table 1; see Section 2), whereas $>50\%$ of the sample was crushed to <100 μm by [16]. However, the different techniques cannot account for the observed scatter, which is more likely due to heterogeneous vesicle densities in the aliquots. An extreme example of this is sample D73-5, which had 18 μcc STP ^{4}He g^{-1} when analyzed by [16], whereas a different split of the same sample analyzed in the Caltech lab contained only 1.1 μcc STP ^{4}He g^{-1}. The difference between the ^{4}He contents can be attributed to a single 1.0 mm diameter vesicle at seafloor pressure present in the aliquot of glass analyzed by Graham et al. [16].

3.2. Neon and argon

Neon and argon isotope ratios and abundances were not determined by [16], therefore no external comparisons are possible. The Ne and Ar isotope ratios, as commonly observed in oceanic basalts, lie between atmospheric compositions and a magmatic end-member defined by high ^{20}Ne/^{22}Ne, ^{21}Ne/^{22}Ne and ^{40}Ar/^{36}Ar. Multiple crushes of the same sample generally result in the highest (least air-like) analyses in the final crushing steps (Table 3, in the **Background Data Set**[1]). Samples that had minor rust-colored alteration tend to have low ^{40}Ar/^{36}Ar and ^{20}Ne/^{22}Ne ratios (Tables 1 and 3).

Relative noble gas abundances are also variable, for example, ^{4}He/^{40}Ar* ratios are between 0.5 and 600. Analyses where the ^{40}Ar/^{36}Ar ratio is indistinguishable from air (typically samples with ^{40}Ar/^{36}Ar ≤ 310 were indistinguishable from the atmospheric value at the 2σ level) allow only an upper limit on the ^{40}Ar* content of the sample and lower limit on the ^{4}He/^{40}Ar* ratio to be calculated by assuming that a ^{40}Ar/^{36}Ar ratio of 310 would result in clearly identifiable ^{40}Ar*. Some individual samples have a significant range in ^{4}He/^{40}Ar*, with the highest ^{4}He/^{40}Ar* ratios typically in the final crushing steps of a particular sample. Some of the final crushing steps are likely compromised by possible He leakage from the partially crushed glass during later crushing steps (see Section 2).

3.3. Carbon dioxide

There are large variations in He/CO_2 ratios within multiple crushing steps of the same sample. These variations must result from the analytical procedures, as it is not likely that the parent magmas are heterogeneous at the centimeter scale: magmatic processes are not likely to fractionate CO_2 from He as they have similar ($<$ factor 2) solubilities in basaltic melt. It has been established that powdering samples in the presence of CO_2 adsorb a significant proportion of the CO_2 [24,27]. It seems likely that the step-crushing procedure used at Caltech results in significant CO_2 adsorption during the final crushing steps when there is a high surface area of glass powder in the crushing apparatus but relatively little CO_2 released. This is consistent with the high He/CO_2 and Ar/CO_2 ratios of the final crushing step of most samples (Table 2, in the **Background Data Set**[1]).

However, if the final crushing steps are not considered, then He/CO_2 ratios are consistent within multiple crushing steps of the same sample. Excluding the final crushing steps, the average reproducibilities of samples that have two or more crushing steps is $\pm 10.5\%$. Considering that the observed variations in He/CO_2 and Ar/CO_2 are a factor of 15 and 10^3, respectively, useful information can be obtained from the manometric CO_2 data.

4. Discussion

There are three possible sources of the large variations in noble gas and CO_2 compositions of these basalts. The mantle source of the basalts may be heterogeneous; vesicle compositions may be affected by magmatic processes; and addition of shallow (crustal or atmospheric) material can mask the magmatic noble gas compositions. The relative importance of each for the ASP basalts is

[1] http://www.elsevier.nl/locate/epsl.

discussed in turn before considering the implications of these processes for oceanic basalts in general.

4.1. Volatiles in the ASP mantle source

Both Ne and Ar isotope ratios are more air-like over the ASP plateau, with elevated $^{20}Ne/^{22}Ne$ and $^{40}Ar/^{36}Ar$ ratios limited to 'normal' ridge segments to either side of the plateau (data not shown). The decrease in $^{40}Ar/^{36}Ar$ in the vicinity of ASP is not thought to reflect changes in mantle Ar isotopic composition: low $^{40}Ar/^{36}Ar$ ratios are accompanied by air-like Ne isotopic composition and the mantle is known to have a non-atmospheric $^{20}Ne/^{22}Ne$ ratio [28,29]. The lower $^{40}Ar/^{36}Ar$ and $^{20}Ne/^{22}Ne$ ratios over the ASP plateau result from an increase in the proportion of atmospheric Ne and Ar in the sample. While there may be variations in these isotope ratios in the mantle source of the basalts [30], these are masked by an increase in the proportion of atmospheric contamination [31,33–37].

4.1.1. Neon

Production of ^{21}Ne in the mantle is predominantly via $^{18}O(\alpha,n)^{21}Ne$ reactions [32]; as O is uniformly distributed through the mantle, the $^{21}Ne/^{22}Ne$ ratio is a function of the time-integrated (U+Th)/^{22}Ne ratio. Similar to He isotope systematics in oceanic basalts, MORBs have more nucleogenic Ne (higher $^{21}Ne/^{22}Ne$ ratios) than OIBs, consistent with lower (U+Th)/Ne as well as lower (U+Th)/He in the mantle source of OIB volcanism.

The majority of the ASP samples have Ne isotope compositions (i.e. the slopes in Fig. 1) that are consistent with those of the MORB source region with $(^{21}Ne/^{22}Ne)_{extr}$ (i.e. extrapolated to a likely mantle $^{20}Ne/^{22}Ne$ of 13.8 [15]) of ≈ 0.07. Less nucleogenic ('less degassed') Ne, as might be expected for a section of ridge with elevated $^{3}He/^{4}He$ ratios, is present in two samples, D39 and D76. Although these two samples have low $(^{21}Ne/^{22}Ne)_{extr}$ values (0.04–0.045), they do not have high $^{3}He/^{4}He$ ratios (Fig. 1). Unfortunately, the majority of samples that do have high $^{3}He/^{4}He$ ratios also erupted at shallow depths and rarely have $^{20}Ne/^{22}Ne$ ratios distinguishable from air.

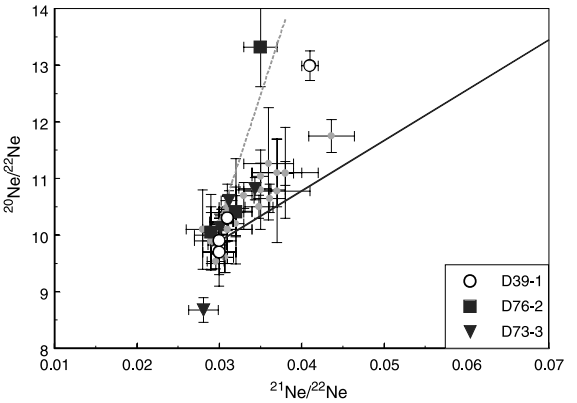

Fig. 1. Ne three-isotope plot. Black line is 'popping rock' data of [36], dashed line is 'DICE' glass [38]. All symbols are analyses from this study; small gray symbols = samples indistinguishable from the MORB trend. Most SEIR samples are broadly consistent with the MORB line, although there is a hint of slightly less nucleogenic Ne in the ASP region. A few samples, highlighted in the legend, have less nucleogenic Ne than the main trend. However, these do not coincide with samples having high $^{3}He/^{4}He$ ratios (e.g. $^{3}He/^{4}He = 7.9$ and 9.4 Ra for D39-1 and D76-2, respectively). By contrast, the sample with the highest $^{3}He/^{4}He$ that has $^{20}Ne/^{22}Ne$ distinguishable from air (D73-3, $^{3}He/^{4}He = 14.4$ Ra) does not have a particularly steep slope in Ne three-isotope space. Although the significant errors preclude a quantitative interpretation, there must be significant variations in $^{3}He/^{22}Ne$ of the respective source regions, with low $^{3}He/^{22}Ne$ coinciding with low (MORB-like) $^{3}He/^{4}He$. This is consistent with interpretations of variable $(^{21}Ne/^{22}Ne)_{extr}$ (see text for definition) for constant $^{3}He/^{4}He$ ratio of oceanic basalts by [15].

4.1.2. Argon

Previous work has shown that it is possible to correct the $^{40}Ar/^{36}Ar$ ratio for atmospheric addition using a four-isotope $^{40}Ar/^{36}Ar$ vs. $^{20}Ne/^{22}Ne$ plot and extrapolating the correlation between $^{40}Ar/^{36}Ar$ and $^{20}Ne/^{22}Ne$ to a mantle $^{20}Ne/^{22}Ne$ ratio [36,39]. However, this correction only applies to systems with two components, air and magmatic noble gases. Alternatively, Turner [40] and Harrison et al. [41] recommend using a three-axis $^{40}Ar/^{22}Ne$–$^{36}Ar/^{22}Ne$–$^{20}Ne/^{22}Ne$ plot to correct for atmospheric addition in order to account for variable Ar/Ne ratios in the atmospheric end-member. However, neither method can be ap-

plied to systems that have fractionated magmatic noble gases. One of the central assumptions behind these corrections is that variations in Ar/Ne result solely from atmospheric contamination (see [41] for more details). Individual samples from the ASP plateau preserve a range in $^{4}He/^{40}Ar^{*}$ that is due to fractionation of noble gases during magmatic degassing (see below). Therefore, there will be variations in Ar/Ne in these samples that are not due to atmospheric addition, and it is not possible to reliably correct $^{40}Ar/^{36}Ar$ for atmospheric addition based on the $^{20}Ne/^{22}Ne$ ratio. Variations in $^{40}Ar/^{36}Ar$ in the source of the ASP basalts cannot be assessed due to the complex and extensive fractionation of the trapped noble gases.

4.1.3. CO_2 and He

Magmatic degassing does not significantly fractionate He from CO_2 because they have broadly similar solubilities in tholeiitic melts (see Section 1; [42,43]), which is consistent with the lack of any correlation between $CO_2/^{3}He$ and a degassing index (such as $^{4}He/^{40}Ar^{*}$; see below) in these samples. Correcting for $CO_2/^{3}He$ fractionation during degassing (using $^{4}He/^{40}Ar^{*}$ as an indication of the extent of magmatic degassing [44]) decreases the overall range in $CO_2/^{3}He$ by only 25% (based on $S_{CO2}/S_{He} = 0.5$, where S = solubility [45]). $CO_2/^{40}Ar^{*}$, on the other hand, is clearly fractionated during magmatic processes and correlates well with $^{4}He/^{40}Ar^{*}$ (Fig. 3b).

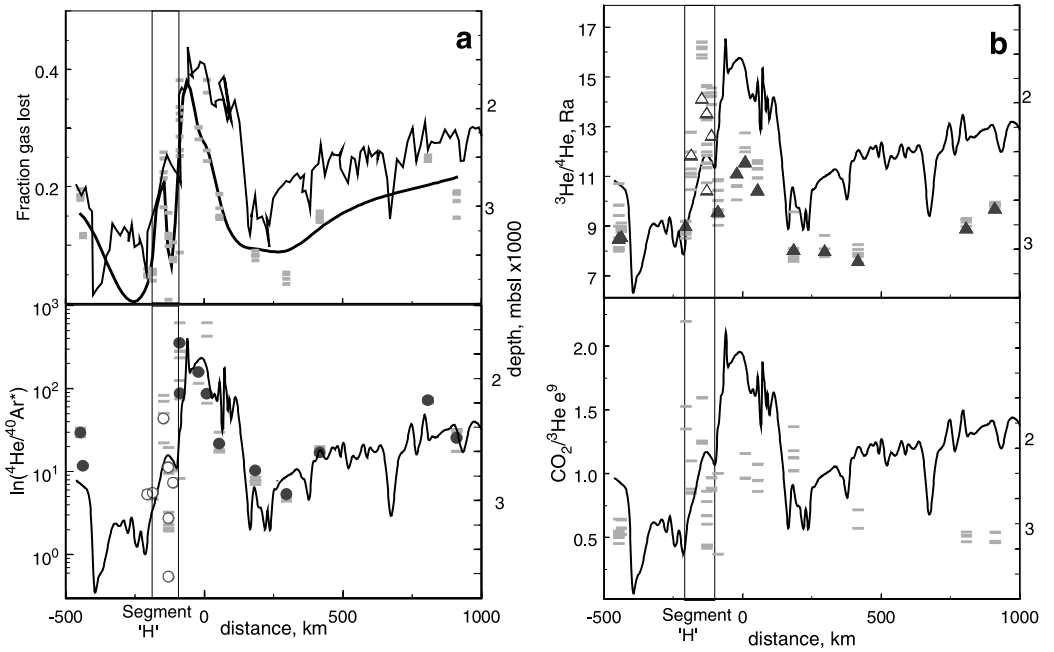

Fig. 2. (a) Degassing and (b) $^{3}He/^{4}He$ and $CO_2/^{3}He$ plotted vs. the distance through the rotation pole of the plate (13.2°N, 38.2°E) from St. Paul Island (38.7°S, 77.55°E). Solid line (right axis) is the ridge depth in km. Circles: sum of all crushing steps of individual samples; solid bars: individual crushing steps; triangles: data from Graham et al. [16]. Individual crushing steps for $CO_2/^{3}He$ only have been plotted as totals and are sensitive to CO_2 adsorbtion in the final crushing stages (see text for details). Open symbols: Segment 'H'. $^{4}He/^{40}Ar^{*}$ (a) can be used as a proxy for degassing, which shows that lavas erupted on the top of the ASP plateau are the most degassed. The fraction gas lost in the top panel is calculated assuming Rayleigh fractionation of a magma that originally had $^{4}He/^{40}Ar^{*} = 2$ and solubilities calculated according to Carroll and Stolper [8]. Noble gas (^{4}He and $^{40}Ar^{*}$) and CO_2 abundances show the same basic pattern, in that the lowest CO_2 abundances are found in the most shallow erupted samples. Segment 'H' does not quite follow the trend, having samples that are both more degassed and less degassed than predicted for a given eruption depth, probably due to some control related to the degree of magmatic differentiation (see also Fig. 4). $CO_2/^{3}He$ is generally lower in samples from normal ridge segments, and higher and more variable across the plateau (totals are not reported for CO_2 as the final step of the crushing process likely adsorbs CO_2; see text).

The order of magnitude variation in $CO_2/^3He$ of the ASP basaltic glasses (Fig. 2b) must therefore represent variations in the primary melt, resulting from changes in source region chemistry, or from changes in melting regime across the ASP plateau. The variation in $CO_2/^3He$ ($\equiv C/^3He$) in these samples, from values similar to the 'canonical' MORB value of $1–2\times10^9$ [43,44] to values approximately one order of magnitude lower, cannot be accounted for by experimental uncertainties (see Section 2). Nishio et al. [46] report similar values and ranges for $CO_2/^3He$ trapped in basalts from the Rodrigues Triple Junction.

There is no clear relationship between $C/^3He$ and basalt chemistry or isotopic composition in the ASP basalts. The lowest $C/^3He$ ratios tend to occur on normal ridge segments to either side of the plateau, but there is no systematic spatial variation in $C/^3He$ as with other tracers ($^3He/^4He$ or K/Ti; Fig. 2). In particular, the entire variation in $C/^3He$ is contained within Segment 'H' and the Zeewolf Fracture Zone (immediately north of Segment 'H'; Fig. 2b). The underlying cause or causes of these large fluctuations in $C/^3He$ over small sections of mid-ocean ridge are not known. While heterogeneities in $C/^3He$ in the source to these basalts may exist, it seems unlikely that large variations in $C/^3He$ in basalts from a single ridge segment (such as Segment 'H') that are not correlated with conventional tracers of mantle heterogeneity ($^3He/^4He$, K/Ti, $^{87}Sr/^{86}Sr$ etc.) can reflect heterogeneities in the mantle source to the ASP basalts. It seems more plausible that the significant fractionation of C from noble gases and from lithophile tracers results either from changes in the melting regime (e.g. fraction of melt generated) or from magmatic processes. These fractionations may be a function of the sensitivity of C speciation to variations in f_{O2} [47] or to kinetic fractionation, resulting from the large differences in noble gas and CO_2 diffusivity in melts. Further work investigating partitioning of volatiles between vesicles and glass in these samples is underway.

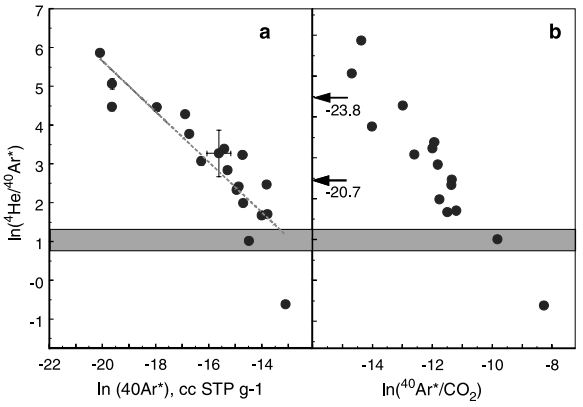

Fig. 3. Linear anti-correlations between $\ln(^4He/^{40}Ar^*)$ and $(^{40}Ar^*)$ and between $\ln(^4He/^{40}Ar^*)$ and $\ln(^{40}Ar^*/CO_2)$ are found in these basaltic glasses. This is predicted for a magma undergoing fractional degassing (assuming that $^{40}Ar^*$ is essentially the same as fraction of gas lost, F in Eq. 1). The slope of the correlation is a function of the relative He and Ar and CO_2 solubilities. The line in (a) is the best fit (least squares) through the data, given by: $\ln(^4He/^{40}Ar^*) = -0.65\pm0.08\ \ln(^{40}Ar^*)-7.35\pm1.27$ ($r^2=0.8$). Likely mantle $^4He/^{40}Ar^*$ production ratio is given by the gray bar. The one sample that has $^4He/^{40}Ar^*$ below production (D73-5) is discussed in the text.

4.2. Degassing

It is clear that $^4He/^{40}Ar^*$ and $^{40}Ar^*/CO_2$ in these samples have been fractionated from their likely initial compositions (Figs. 2 and 3; Table 2). This fractionation can be plausibly attributed to solubility-controlled degassing during magma ascent and eruption. The extent of fractionation (the high $^4He/^{40}Ar^*$ ratios) cannot be generated by batch degassing. During batch degassing, each episode of gas loss increases the $^4He/^{40}Ar^*$ ratio by a maximum of the ratio S_{He}/S_{Ar}. It is difficult to construct a realistic batch degassing mechanism that can account for the $\approx$200 times enrichment of He relative to Ar in some of these samples (max $^4He/^{40}Ar^*=620$; initial $^4He/^{40}Ar^*\approx3$) given that $S_{He}/S_{Ar}\approx10$. It is more appropriate to model gas loss from these magmas as a fractional (or near-fractional) process.

During fractional degassing, the concentrations of residual magmatic gases (C) are related to the fraction of volatiles lost (F) by:

$$\frac{C_i}{C_j}=\left(\frac{C_i}{C_j}\right)_0 F_i^{(1-\alpha_{i,j})} \quad (1)$$

where $\alpha_{i,j}$ is the ratio of solubilities of species i and j [6].

The pattern of gas loss (Fig. 3) is consistent with solubility-controlled Rayleigh (fractional) degassing as the dominant fractionating mechanism. The one exception to this is sample D73-3 that has a $^4He/^{40}Ar^*$ ratio of 0.5, clearly lower than the production ratio of 2–4 (see Section 1): degassing will increase the He/Ar ratio of the residual volatiles. Therefore:

1. either the volatiles in D73-3 are not the *residual* volatiles of degassing, but represent the first bubbles formed from the magma, or
2. some other non-equilibrium process such as post-eruptive He loss where high He diffusivities (relative to Ar) in cooling glasses may have resulted in the low He/Ar ratio in this sample.

This sample has the highest MgO content of the sample suite. Although it is not possible to discount post-eruptive He loss from the sample, it seems possible that the first generation of bubbles could be preserved in the least evolved samples such as D73-3, while more evolved lavas lost their early formed bubbles. The He/Ar ratio of the bubbles depends on vesicularity in addition to the melt He/Ar ratio because little fractionation occurs at high vesicularities when virtually all the He and Ar is present in the large volume fraction of bubbles. In order to significantly fractionate He from Ar to generate the $^4He/^{40}Ar^*$ of 0.5 in the vesicles of D73-3, a low vesicularity is required; assuming $S_{He}/S_{Ar} = 10$, a vesicularity of less than 0.1% will result in $(^4He/^{40}Ar^*)_{ves} = 0.5$ in equilibrium with a melt with $^4He/^{40}Ar^* = 3$ (following [6,21]).

4.2.1. *He and Ar solubilities during degassing of ASP magmas*

From Eq. 1 and the slope of the correlation between $[^{40}Ar^*]$ and $^4He/^{40}Ar^*$ (slope = -0.65 ± 0.08; Fig. 3 caption), S_{He}/S_{Ar} must lie between 4.07 and 8.52 for this suite of basalts. This compares reasonably well with experimentally determined solubilities, for example, the ionic porosity model of Carroll and Stolper [8] suggests that S_{He}/S_{Ar} is in the range 6.7–12.3 for basalts of the compositions found here (and neglecting corrections for degassing at high pressures [48] and for volatile composition on noble gas fugacity [49]).

Modeling fractionation of He from Ne and Ar in MORB glasses, Moreira and Sarda [50] stated that experimentally determined He, Ne and Ar solubilities could not account for the observed compositions. Instead, $S_{He}/S_{Ar} > 40$ was required to explain significant fractionation of He from Ar for a given He/Ne ratio. However, their model was based on batch degassing of magmatic gases. The high $^4He/^{40}Ar^*$ ratios in the ASP basaltic glasses are difficult to model as a batch degassing process, suggesting that fractional or near-fractional gas loss occurs on this section of the SEIR. The He–Ar systematics are entirely consistent with experimentally determined solubilities.

4.2.2. *Initial gas contents of ASP magmas*

The gas contents of the magma prior to degassing can be estimated by extrapolating the trend in Fig. 3 to a likely mantle $^4He/^{40}Ar^*$ of between 2 and 4 [9,10]. From the best fit (least squares) to the data in Fig. 3, the initial $^{40}Ar^*$ concentration in the magma prior to any gas loss was between 1.5 and 4.3 μcc STP g^{-1}, corresponding to ^4He concentrations in the magma of between 5.9 and 8.6 μcc STP g^{-1}. This is consistent with the highest He concentrations that have been measured in these basalts (excluding one aliquot of D73-5; see Section 3). Note that all samples fall on the same trend irrespective of $^3He/^4He$ ratio; high $^3He/^4He$ samples do *not* project to a higher initial $^{40}Ar^*$ or ^4He.

Independent estimates of ^4He concentrations in undegassed MORB magmas are typically at least a factor of three higher than these estimates. For example, the global He flux from mid-ocean ridges is relatively well constrained at $1–2 \times 10^{12}$ cc STP ^4He yr^{-1} (based on 500–1000 mole ^3He yr^{-1} with $^3He/^4He = 8$ Ra [51–53]), while the minimum MOR crustal production rate is ≈ 15 km^3 yr^{-1}, providing a minimum ^4He content of MORB magmas of 25–50 μcc STP g^{-1}. This is a minimum estimate as it assumes 100% outgassing efficiency of MORB magmas during crustal accretion. Alternatively, it is common to assume that initial magmatic He contents are similar to

those of the most gas-rich MORB glass ('popping rock') of 50–90 μcc STP g^{-1} [36,54]. Both estimates are higher than the initial He (or Ar) concentrations of the ASP basaltic glasses. While the uncertainties in all estimates of noble gas concentrations are large, it is unlikely the uncertainties can account for the discrepancy between the initial He and Ar contents of the ASP magmas and independent estimates.

The reason for the discrepancy between our estimate of undegassed magmatic He contents and independent estimates is unclear. Basaltic glasses probably do not retain 100% of the noble gases that are present on eruption due to vesicle rupture during sample recovery and/or preparation [27]. While low crushing efficiency in the present study results in a low apparent noble gas concentration (see Section 2), this only results in a decrease of 20–30%. In order for post-eruptive vesicle loss to account for the low noble gas concentrations in these samples relative to independent estimates then:

1. if the initial ^{4}He concentration was 25 μcc g^{-1} (the lowest independent estimate), at least 65% of the gases must have been lost by post-eruptive vesicle loss;
2. both He and Ar must have been lost equally, suggesting that vesicle rupture rather than noble gas diffusion would have to result in the low observed concentrations; and
3. a near-constant gas fraction must have been lost from each sample (i.e. every sample must have lost $\approx$65% of their gases with little sample-to-sample variation), otherwise there would not be a correlation between ^{4}He/^{40}Ar* and [^{40}Ar*] between samples.

It seems more likely that the comparatively low noble gas concentrations in these basaltic glasses do reflect low concentrations in the parent magmas. Either estimating He concentrations using the He outgassing flux is somehow flawed, or the noble gas content of the MORB mantle source region is heterogeneous and these basalts sample a region of the mantle that is particularly noble gas-deficient. However, given that ^{3}He/^{4}He ratios do not support long-lived ^{3}He/(U+Th) heterogeneities in the MORB mantle this seems unlikely. In fact, high ^{3}He/^{4}He segments of mid-ocean ridges – such as the ASP plateau – are more likely sourced from *high* noble gas/(U, Th, K) regions of the mantle (see Section 1). Another possibility is that noble gas concentrations in primary melts are sensitive to kinetic processes during melting (e.g. [55]), although there are no quantitative models of how these will affect noble gas abundances or abundance ratios. As a result, the factors controlling noble gas abundances in oceanic basalts are not well understood.

4.3. Cause of degassing

While it is clear that fractional degassing can account for the volatile compositions observed in these basalts, the cause or timing of the fractional degassing is not constrained. Two end-member scenarios can be envisaged to account for the volatile fractionation seen in these magmas:

1. The volatile phase is largely preserved by the magma during residence in and transport through the crust, with large-scale gas loss and volatile fractionation only occurring on rapid decompression during eruption; or
2. volatiles are continuously lost from the magma as it crystallizes [44].

4.3.1. Decompression during eruption and degassing

The extent of degassing in (1) above would be related to the amount of decompression experienced by the sample during eruption (although kinetic effects may be important [56]). The most significant control on eruption decompression is the eruption depth, with the maximum decompression, and therefore most degassing, occurring in the most shallowly erupted lavas [23]. Using the ^{4}He/^{40}Ar* ratio as a proxy for the extent of degassing, it is clear that there is a relationship between the amount of degassing and ridge (i.e. eruption) depth, with the most shallowly erupted samples having lost the largest fraction of gas (Figs. 2 and 4). Some samples, particularly those from Segment 'H', do not fit this pattern, with a large range in ^{4}He/^{40}Ar* at a near-constant eruption depth. It is possible to model the variation in ^{4}He/^{40}Ar* with eruption depth as a constant fraction of CO_2 lost from each sample for a given

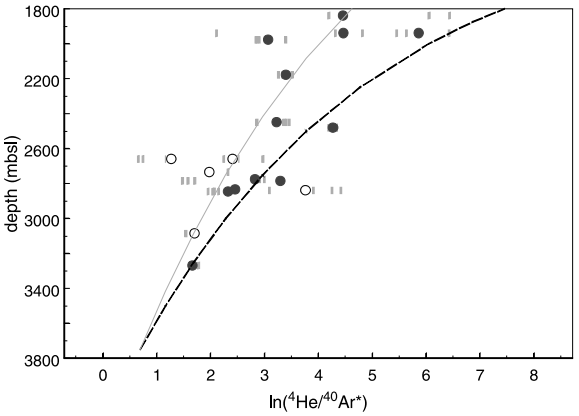

Fig. 4. $^{4}He/^{40}Ar^{*}$ as a function of ridge depth. Symbols as in Fig. 2. Segment 'H' does not follow the main degassing trend, as may be expected for a glass that preserves vesicles from different stages of degassing. If eruption depth is the main control on extent of degassing, then it is possible to model these degassing curves as a simple Rayleigh process. The dashed line and solid lines are models of 4% and 3% CO_2 lost for a decrease in ridge depth of 100 m ($\approx$10 bar reduction in confining pressure), starting with no gas loss at 3750 m, then 3 or 4% CO_2 is lost at 3650 m, then a further 3 or 4% of the remaining CO_2 is lost at 3550 m etc. He and Ar partition between the vapor and melt according to Eq. 1. Relative He and Ar solubilities calculated from [8].

decrease in eruption depth (Fig. 4). Using published noble gas solubilities, the data are bracketed by the fractionation predicted if between 3 and 4% of the CO_2 is lost for each 100 m ($\approx$10 bar) decrease in eruption pressure, assuming fractional degassing (Fig. 4). However, the large range in $^{4}He/^{40}Ar^{*}$ at near-constant eruption depth (for example, on Segment 'H') shows that there are other controls on volatile fractionation than merely eruption pressure, as discussed in the following section.

4.3.2. *Degassing during fractional crystallization*

An important model recently developed by Marty and Zimmerman [44] has shown how relationships between MgO and $^{4}He/^{40}Ar^{*}$ in MORBs globally could be due to volatile loss as a result of fractional crystallization if CO_2 behaves as an incompatible element. Bubbles of CO_2 will form in crustal magma chambers, fractionating He from Ar (see Section 1). The amount of CO_2 that is lost at this stage depends on the initial CO_2 content and pressure of the magma: shallow magmas and high initial CO_2 contents promote a higher fraction of CO_2 in bubbles. Reasonable estimates of initial CO_2 contents ($\approx$1000 ppm [47]) and magma chamber pressures (1–3 kbar [57]) suggest that between 0 and 40% of the CO_2 will form bubbles at this stage, resulting in a maximum $^{4}He/^{40}Ar^{*}$ of $\approx$40 (assuming the 40% CO_2 is lost fractionally) in the residual magma, considerably lower than the maximum measured in the ASP samples.

If these bubble are lost from the magma, then the magma remains in equilibrium with CO_2 solubility at the (lithostatic) pressure, so no further gas will be lost and no further He/Ar fraction will occur (provided there is no decrease in pressure). However, if fractional crystallization occurs, then, because CO_2 behaves incompatibly, the effective concentration of CO_2 in the magma will increase. The new CO_2 concentration exceeds its solubility limit at the magma chamber pressure, therefore further CO_2 will exolve, fractionating the He/Ar ratio further. As a result, a negative correlation between a volatile fractionation index (He/Ar) and a crystal fractionation index (e.g. MgO) is predicted [44]. In addition, this model predicts a positive correlation between the concentrations of incompatible elements and the He/Ar ratio. The He/Ar fractionation is an exponential function of the fraction CO_2 above solubility ($\equiv$fraction CO_2 lost; Eq. 1), therefore log–linear relationships between $^{4}He/^{40}Ar^{*}$ and the basalt major and trace element concentrations are predicted.

Fig. 5 shows that there are good correlations between volatiles and crystal fractionation, with $^{4}He/^{40}Ar^{*}$ and $[^{40}Ar^{*}]$ concentrations increasing exponentially as the MgO content of the lavas decreases, because, in general, MgO decreases over the ASP plateau. It is possible to satisfactorily model the evolution of $^{4}He/^{40}Ar^{*}$ as a function of MgO content for a crystallizing, degassing magma at pressures between 2 and 4 kbar using published initial CO_2 contents (of 1000 ppm) and published CO_2 and noble gas solubilities (see Fig. 5 caption for more details). While the initial CO_2 content of oceanic basalts is not well known and it is possible that these basalts have low initial

CO_2 contents (consistent with low initial $^{40}Ar^*$ contents; see Section 4.2.2), this does not invalidate the model. A low initial CO_2 content would simply require that degassing occurred at lower pressure in order that the magma become saturated with respect to CO_2. For example, if the initial CO_2 content was 600 ppm, then the MgO–$^4He/^{40}Ar^*$ relationship can be reproduced for a magma chamber at 1.5 kbar. Correlations between TiO_2 and $^4He/^{40}Ar^*$ are also consistent with those predicted for a crystallizing, degassing magma (Fig. 6). In these plots, the samples from Segment 'H' cannot be distinguished from the overall trend, in contrast to the plot of $^4He/^{40}Ar^*$ vs. depth (Fig. 4). Fractional crystallization therefore appears to play a more important role in determining the fraction of gas lost from a magma than eruption depth for Segment 'H' basalts, if not for all ASP basalts.

4.4. Assimilation and contamination

Atmospheric noble gases are inevitably present during analyses of basaltic glasses [33]. The concentration of magmatic gases, particularly of [$^{40}Ar^*$] in basaltic glasses, varies with both eruption depth (Fig. 4) and magmatic differentiation (Fig. 5), therefore the measured $^{40}Ar/^{36}Ar$ ratio of a basaltic glass is unlikely to reflect that of its source region. Coincidental relationships between $^{40}Ar/^{36}Ar$ and trace element or isotopic tracers of mantle source [30] are unlikely to be meaningful.

Marty and Zimmerman [44] and Fisher [55,58] proposed that assimilation of ^{36}Ar-bearing crust could account for low $^{40}Ar/^{36}Ar$ ratios of some oceanic basalts. This is inconsistent with measured noble gas compositions that show the atmospheric contaminants are not located in the same site as the magmatic gases, viz. ^{36}Ar in basaltic

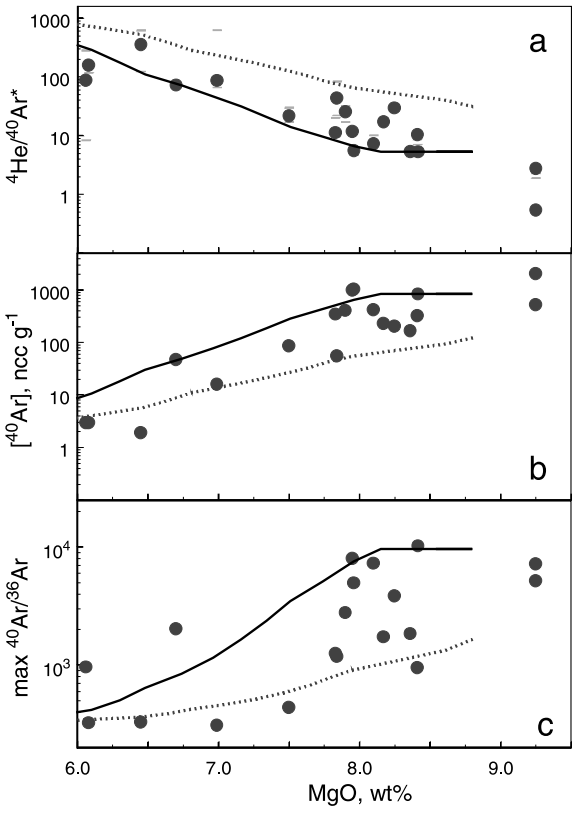

←

Fig. 5. Fractional crystallization and degassing. $^4He/^{40}Ar^*$ broadly correlates with MgO content (plot a) of the basalts, indicating that degassing – as traced by He/Ar – is accompanied by fractional crystallization – as traced by MgO. Log–linear relationships are expected because He/Ar fractionates exponentially (Eq. 1). Predicted compositions are shown for 2 kbar (dotted line) and 3 kbar (solid line) combined fractional crystallization and degassing. The starting composition used for the model is that of D75-1 (He/Ar and major elements) and assuming an initial CO_2 content of 1000 ppm. Note that initial CO_2 content trades off with pressure of degassing because the $^4He/^{40}Ar^*$ ratio is determined by the fraction of CO_2 above its solubility limit. The He and Ar solubilities used are those calculated according to Carroll and Stolper [8] for the composition of D75 ($S_{He}/S_{Ar} = 12$) but do not vary with basalt composition. CO_2 solubility is that of [68]. The model satisfactorily reproduces the overall $^4He/^{40}Ar^*$ (a) and $^{40}Ar^*$ (b) concentrations. The variation in the maximum $^{40}Ar/^{36}Ar$ measured in these basalts can be adequately described by degassing followed by contamination by a fixed amount of ^{36}Ar (c): the lines in the figure are the $^{40}Ar/^{36}Ar$ ratios that would result from adding 1.2×10^{-12} cc STP atmospheric Ar ($^{40}Ar/^{36}Ar = 295.5$) per gram of basalt that has a $^{40}Ar^*$ content as described in (b). No assimilation of ^{36}Ar-bearing crustal material is required to account for the data. The scatter observed in (c) is not surprising, as the atmospheric contaminant is unlikely to be constant but more likely is a function of the surface area, in turn dependent on the quality of the basaltic glass being analyzed.

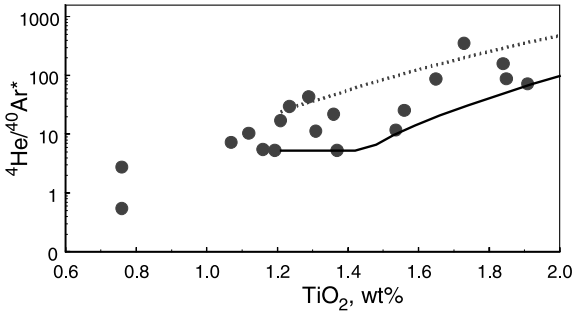

Fig. 6. Combined fractional crystallization/degassing can also account for correlated variations between degassing index (e.g. $^4He/^{40}Ar^*$, although $^{40}Ar^*/CO_2$ displays similar patterns) and incompatible elements such as Ti. Lines are for modeled fractional crystallization/degassing as in Fig. 5.

glasses is not in the vesicles [35,59]. If ^{36}Ar was introduced into the magma by assimilation, then it would be expected to partition between the glass and vesicles, contrary to the observations of [35,59].

There is no correlation between ^{36}Ar and MgO content in these ASP glasses; ^{36}Ar contents do not increase in shallowly erupted, evolved lavas on the ASP plateau. There is a broad relationship between MgO and the maximum $^{40}Ar/^{36}Ar$ ratio measured in the samples such that high $^{40}Ar/^{36}Ar$ ratios are limited to samples with more than 8 wt% MgO (Fig. 5c). However, the relationship (albeit poor) between $^{40}Ar/^{36}Ar$ and MgO does not require that the amount of ^{36}Ar assimilated from the surrounding crust controls the $^{40}Ar/^{36}Ar$ ratio. Rather, the ^{40}Ar content decreases with MgO content due to degassing during crystallization, and the addition of a near-constant atmospheric contaminant to these samples (for example, a persistent surface-adsorbed component that is not removed during baking) will result in a non-causal relationship between $^{40}Ar/^{36}Ar$ and MgO as seen in Fig. 5c. There is considerably more variability in $^{40}Ar^*$ concentration (factor of $>10^3$ total variation in concentration) than in ^{36}Ar concentration (total variation = 72) in these samples, consistent with the extent of degassing, rather than the extent of contamination, as the main control on $^{40}Ar/^{36}Ar$.

Assimilation of surrounding crust clearly does occur in MOR magmas [60]. In order that the ^{36}Ar budget is dominated by adsorbed atmospheric contaminants as opposed to assimilated crustal ^{36}Ar, the ^{36}Ar concentration of the oceanic crust at the depths where magmatic crystallization occurs in the ASP samples (i.e. 4–12 km [26]) must be low; using a typical magma:assimilant ratio of 10:1, the ^{36}Ar concentration of the assimilated material must be $<1\times10^{-12}$ cm^3 STP g^{-1}, otherwise the effects of assimilation would be evident in the ^{36}Ar concentrations.

4.5. Degassing and mixing

Graham et al. [16] observed that ASP basalts do not display simple binary mixing in $^3He/^4He$ vs. K/Ti space, rather there is a range in He/Ti in the magmatic end-members of more than 50 (see Section 1). The basalts with the highest $(He/Ti)_{EM}/(He/Ti)_{DM}$ ratios did not erupt on the main portion of the plateau, but on a ridge segment (Segment 'H') at normal depth (2700 m below sea level) immediately west of the plateau [16]. From the He–K/Ti mixing systematics, He contents of the high $^3He/^4He$ magma are generally within a factor of two of those of the low $^3He/^4He$ magma. By contrast, the high $^3He/^4He$ magmas in Segment 'H' likely had He concentrations up to 50 times higher than the MORB-like magma along this segment (i.e. from mixing systematics, $(He/Ti)_{EM}/(He/Ti)_{DM}\approx50$ and Ti content is assumed to be relatively constant). This was thought by [16] to reflect the fact that He had been efficiently extracted from the mantle beneath the central portion of the plateau ('mined') by the extensive magmatism that produced the plateau.

The lowest $^4He/^{40}Ar^*$ ratios are also found in Segment 'H' basalts. It is possible to contour $^3He/^4He$ vs. K/Ti (figure 3 of [16]) for $^4He/^{40}Ar^*$ (Fig. 7). This allows the relationship between the r value and the extent of degassing to be investigated. Degassed samples with high $^4He/^{40}Ar^*$ have low r values and plot in the central portion of the $^3He/^4He$ vs. K/Ti diagram, whereas low $^4He/^{40}Ar^*$ ratios are limited to either the high r quadrant of the mixing space (top left of Fig. 7), or to regions close to the end-member compositions (where there is no control on the r coefficient).

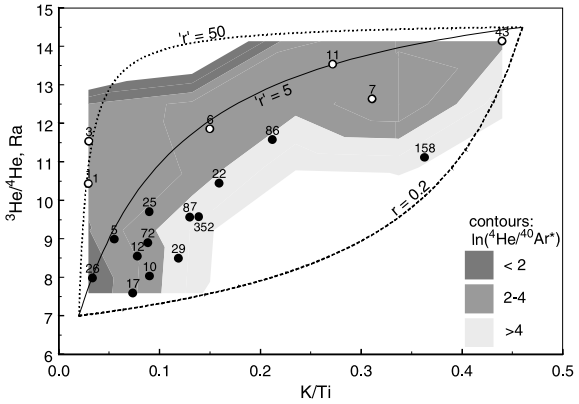

Fig. 7. He isotopes vs. K/Ti (after [16]), contoured for $^{4}He/^{40}Ar^{*}$. Circles: data with $^{4}He/^{40}Ar^{*}$; open circles: Segment 'H' samples. Numbers next to symbols are the $^{4}He/^{40}Ar^{*}$ ratios for that sample. Mixing between an enriched, high $^{3}He/^{4}He$ magma ($^{3}He/^{4}He = 14$ Ra, K/Ti = 0.45) and a depleted, MORB-like magma ($^{3}He/^{4}He = 7$ Ra, K/Ti = 0.02) is modeled (lines) with the curvature of the mixing lines (r) given by $(He/Ti)_{EM}/(He/Ti)_{DM}$. It is clear that the data do not lie on a mixing line with a single value of r, rather there must be a range in $(He/Ti)_{EM}/(He/Ti)_{DM}$. Samples that plot on mixing lines with low r tend to have high $^{4}He/^{40}Ar^{*}$, whereas high r samples have low $^{4}He/^{40}Ar^{*}$.

From Fig. 7, it appears that the $(He/Ti)_{EM}/(He/Ti)_{DM}$ is related to the degree of degassing (as traced by $^{4}He/^{40}Ar^{*}$), with low $(He/Ti)_{EM}/(He/Ti)_{DM}$ samples restricted to degassed samples. Depletion of He in the mantle source to the basalts – 'He mining' – is not required to account for the observations. The variation in $(He/Ti)_{EM}/(He/Ti)_{DM}$ results from variable degrees of gas loss from a magma *prior* to mixing with a second batch of magma with different $^{3}He/^{4}He$ and K/Ti. This may, for example, represent a continuously fractionating–degassing–replenishing system where a chamber or melt lens containing degassed and fractionated magma is periodically supplied by fresh, undegassed melt. Mixing systematics of samples that have unfractionated He/Ar ratios (e.g. D73-4 and D73-5) suggest that $(He/Ti)_{EM}/(He/Ti)_{DM} \geq 20$ prior to degassing.

4.5.1. Global mixing systematics

The He concentrations measured in basalt glasses from ocean islands with high $^{3}He/^{4}He$ ratios are lower than the concentrations in ocean ridge basalt glasses which have lower and relatively uniform $^{3}He/^{4}He$ ratios [61–63]. Also, mixing systematics between $^{3}He/^{4}He$ ratios and trace element (e.g. La/Sm) or isotopic (e.g. $^{87}Sr/^{86}Sr$) indicators of enrichment in oceanic basalts are not usually consistent with high He concentrations in high $^{3}He/^{4}He$ basalt magmas [13,64–67]. Rather, the curvature of mixing lines suggests that the He concentrations in magmas that have high $^{3}He/^{4}He$ and magmas that have MORB-like $^{3}He/^{4}He$ are broadly similar. These observations (dubbed 'The Helium Paradox' [62]) are inconsistent with most models of terrestrial $^{3}He/^{4}He$ evolution that require high $^{3}He/U$ ratios (and high He concentrations) for long periods of time in the source of high $^{3}He/^{4}He$ OIBs (see Section 1).

The results of this study suggest that mixing systematics between He isotopes (or any other noble gas) and lithophile tracers are unlikely to reflect noble gas contents of the mantle source to that magma, because noble gases are lost from magmas *prior* to mixing. Noble gas concentrations, and therefore the mixing systematics involving noble gas isotopes, instead are determined by the fraction of CO_2 lost from the magma before mixing. The fact that there are usually near-linear mixing trajectories for He isotopes vs. La/Sm, $^{206}Pb/^{204}Pb$ or $^{87}Sr/^{86}Sr$ suggests that the fraction of CO_2 lost from the magma is broadly the same (compared to the factor 1000 variation in noble gas concentrations) irrespective of the mantle source region. The fraction CO_2 lost is largely a function of initial CO_2 content and the pressure of combined fractional crystallization/degassing, implying that either there is a trade-off between the two parameters (e.g. high CO_2 magmas crystallize and degas at higher pressure) or that initial CO_2 content and the pressure of combined crystallization–degassing does not vary significantly for all oceanic basalts.

The importance of combined fractional crystallization and degassing in determining noble gas absolute and relative abundances in oceanic basaltic glasses worldwide is difficult to assess due to the lack of noble gas and basalt composition data on the same samples. Combined fractional crystallization and degassing will be sensitive to variables such as initial CO_2 content and pressure(s)

of fractional crystallization. As a result, it seems doubtful there will be a single, well defined curve between $^4He/^{40}Ar^*$ and MgO for all MORB glasses. The recent work by Marty and Zimmerman [44] shows that – with scatter – fractional crystallization and degassing is generally applicable to some ocean basins. However, our preliminary data for basaltic glasses from the SEIR east of the ASP Plateau to the Australian–Antarctic discordance (120°E) are inconsistent with fractional crystallization as the primary control on degassing of basaltic magmas; some other as yet unknown process or processes also appears to determine the extent of degassing in MORBs (manuscript in preparation).

5. Conclusions

With the exception of He (and possibly Ne) isotopes, the composition of noble gases trapped in ASP Plateau basaltic glasses is primarily controlled by magmatic degassing and late-stage contamination by atmospheric components. The absolute and relative noble gas abundances are consistent with fractional degassing, with noble gas solubilities similar to experimentally determined values. The extent of gas loss increases with increasing fractional crystallization, resulting in low $^{40}Ar^*$ concentrations and high $^4He/^{40}Ar^*$ in evolved basalts. The relationship between crystallization (e.g. MgO) and degassing (e.g. $^{40}Ar^*$ or $^4He/^{40}Ar^*$) can be satisfactorily reproduced assuming that CO_2 behaves incompatibly, therefore is lost during crystallization of the magma. The most degassed (and also most evolved) basalts occur on the shallowest part of the ASP plateau. As a result, it is not possible to eliminate eruption depth as a potential control on extent of gas loss, although large variations in $^4He/^{40}Ar^*$ with minor variation in eruption depth in Segment 'H' basalts suggest that (for these basalts at least), eruption depth is a secondary control on fraction CO_2 degassed. $^{40}Ar/^{36}Ar$ ratios are consistent with addition of a near-constant atmospheric contaminant ($^{40}Ar/^{36}Ar = 300$) to magmatic Ar with $^{40}Ar/^{36}Ar \geq 10\,000$.

The initial noble gas concentrations can be estimated by extrapolating correlations with $^4He/^{40}Ar^*$ to the likely mantle $^4He/^{40}Ar^*$ of between 2 and 4. The initial He concentrations estimated using this technique (5.9–8.6 μcc STP g^{-1}) are significantly lower than those of the 'popping rock' (50–90 μcc STP g^{-1}) or of estimates based on He fluxes through mid-ocean ridges (≥ 25 μcc STP g^{-1}).

From this study, it is clear that noble gases can be lost from magmas prior to magmatic fractionation and mixing of magmas with different chemical or isotopic compositions. As a result, correlations between noble gas isotopes and lithophile tracers will be controlled by the extent of degassing at the time of mixing: the curvature of mixing diagrams involving noble gases will *not* reflect the pre-degassing noble gas concentrations of the mantle source to oceanic basalts.

Acknowledgements

This work was supported by the Marine Geology and Geophysics program of the NSF. Discussions with Bernard Marty were valuable in formulating the ideas behind this study, and reviews by Bernard Marty and Chris Ballentine considerably improved the final manuscript. ***[BOYLE]***

References

[1] W.B. Clarke, M.A. Beg, H. Craig, Excess 3He in the sea: evidence for terrestrial primordial He, Earth Planet. Sci. Lett. 6 (1969) 213–220.
[2] B.A. Mamyrin, I.N. Tolstikhin, G.S. Anufriev, I.L. Kamanskiy, Anomalous isotopic composition of He in volcanic gases, Dokl. Akad. Nauk SSSR 184 (1969) 1197–1199.
[3] K.A. Farley, E. Neroda, Noble gases in the Earth's mantle, Annu. Rev. Earth Planet. Sci. 26 (1998) 189–218.
[4] S.J.G. Galer, R.K. O'Nions, Residence time of thorium, uranium and lead in the mantle with implications for mantle convection, Nature 316 (1985) 778–782.
[5] V. Pan, J.R. Holloway, R.L. Hervig, The pressure and temperature dependence of carbon dioxide solubility in tholeiitic basalt melts, Geochim. Cosmochim. Acta 55 (1991) 1587–1595.
[6] A. Jambon, H. Weber, O. Braun, Solubility of He, Ne, Ar, Kr and Xe in a basalt melt in the range 1250–1600°C.

Geochemical implications, Geochim. Cosmochim. Acta 50 (1986) 401–408.
[7] G. Lux, The behavior of noble gases in silicate liquids: solution, diffusion, bubbles and surface effects, with applications to natural samples, Geochim. Cosmochim. Acta 51 (1987) 1549–1560.
[8] M.R. Carroll, E.M. Stolper, Noble gas solubilities in silicate melts and glasses: new experimental results for argon and the relationship between solubility and ionic porosity, Geochim. Cosmochim. Acta 57 (1993) 5039–5052.
[9] A. Jambon, H.W. Weber, F. Begeman, Helium and argon from an Atlantic MORB glass: concentration, distribution and isotopic composition, Earth Planet. Sci. Lett. 73 (1985) 255–267.
[10] C.J. Allègre, T. Staudacher, P. Sarda, Rare gas systematics: formation of the atmosphere, evolution and structure of the Earth's mantle, Earth Planet. Sci. Lett. 81 (1986) 127–150.
[11] D.W. Graham, Helium isotope variations along mid-ocean ridges; mantle heterogeneity and melt generation effects, Mineral. Mag. 58A (1994) 347–348.
[12] D.W. Graham, W.J. Jenkins, J. Schilling, G. Thompson, M.D. Kurz, S.E. Humphris, Helium isotope geochemistry of mid-ocean ridge basalts from the South Atlantic, Earth Planet. Sci. Lett. 110 (1992) 133–147.
[13] D.W. Graham, P.R. Castillo, J.E. Lupton, R. Batiza, Correlated He and Sr isotope ratios in the South Atlantic near-ridge seamounts and implications for mantle dynamics, Earth Planet. Sci. Lett. 144 (1996) 491–503.
[14] S. Niedermann, W. Bach, J. Erzinger, Noble gas evidence for a lower mantle component in MORBs from the southern East Pacific Rise: Decoupling of helium and neon isotope systematics, Geochim. Cosmochim. Acta 61 (1997) 2697–2715.
[15] M. Moreira, T. Staudacher, P. Sarda, J.-G. Schilling, C.J. Allègre, A primitive plume neon component in MORB: the Shona Ridge anomaly, South Atlantic (51–52° South), Earth Planet. Sci. Lett. 133 (1995) 367–377.
[16] D.W. Graham, K.T.M. Johnson, L.D. Priebe, J.E. Lupton, Hotspot-ridge interaction along the Southeast Indian Ridge near Amsterdam and St. Paul islands: helium isotope evidence, Earth Planet. Sci. Lett. 167 (1999) 297–310.
[17] K.T.M. Johnson, D.W. Graham, K.H. Rubin, K. Nicolaysen, D.S. Scheirer, D.W. Forsyth, E.T. Baker, L.M. Douglas-Priebe, Boomerang Seamount; the active expression of the Amsterdam-St. Paul Hotspot, Southeast Indian Ridge, Earth Planet. Sci. Lett. 183 (2000) 245–259.
[18] K.O. Nicolaysen, K.T.M. Johnson, D. Graham, J. Mahoney, F. Frey, Ridge-hotspot interaction in the southern Indian Ocean: evidence from Sr, Nd and Pb isotopic compositions of Southeast Indian Ridge basalts, EOS 81 (2000) F1129.
[19] C.H. Langmuir, R.D. Vocke, G.N. Hanson, S.R. Hart, A general mixing equation with applications to Icelandic basalts, Earth Planet. Sci. Lett. 37 (1978) 380–392.
[20] P.G. Burnard, F.M. Stuart, L. Ayliffe, G. Turner, C. Curtis, Combined noble gas and quadrupole mass spectrometer analysis of volatiles trapped in fluid inclusions, in: Y.K. Kharakha, A.S. Maest (Eds.), Water–Rock Interaction, Balkema, Rotterdam, 1992, pp. 903–906.
[21] P.G. Burnard, The bubble-by-bubble volatile evolution of two mid-ocean ridge basalts, Earth Planet. Sci. Lett. 174 (1999) 199–211.
[22] M. Javoy, F. Pineau, The volatiles record of a 'popping' rock from the Mid-Atlantic Ridge at 14°N: chemical and isotopic composition of gas trapped in the vesicles, Earth Planet. Sci. Lett. 107 (1991) 598–611.
[23] J.G. Moore, Vesicularity and CO2 in mid-ocean ridge basalt, Nature 282 (1979) 250–253.
[24] C. Barker, B.E. Torkelson, Gas adsorption of crushed quartz and basalt, Geochim. Cosmochim. Acta 55 (1975) 212–218.
[25] P.G. Burnard, K.A. Farley, Calibration of pressure-dependent sensitivity and discrimination in Nier-type noble gas ion sources, Geochem. Geophys. Geosyst. (2000) 2000GC000038.
[26] L.M. Douglas-Priebe, Geochemical and petrogenetic effects of the interaction of the Southeast Indian Ridge and the Amsterdam-St. Paul hotspot, M.S. Thesis, Oregon State University, 1998.
[27] P.G. Burnard, D. Harrison, G. Turner, R. Nesbitt, The degassing and contamination of noble gases in mid-Atlantic Ridge basalts, Geochem. Geophys. Geosyst. (in press).
[28] P. Sarda, T. Staudacher, C. Allègre, Neon isotopes in submarine basalts, Earth Planet. Sci. Lett. 91 (1988) 73–88.
[29] M. Honda, I. McDougall, D.B. Patterson, A. Doulgeris, D.A. Clague, Possible solar noble-gas component in Hawaiian basalts, Nature 349 (1991) 149–151.
[30] P. Sarda, M. Moreira, T. Staudacher, Argon-lead isotopic correlation in Mid-Atlantic Ridge basalts, Science 283 (1999) 666–668.
[31] P.G. Burnard, Origin of argon-lead isotopic correlation in basalts, Science 286 (1999) 871.
[32] I. Yatsevich, M. Honda, Production of nucleogenic neon in the Earth from natural radioactive decay, J. Geophys. Res. 102 (1997) 10291–10298.
[33] P.G. Burnard, D.W. Graham, G. Turner, Vesicle-specific noble gas analyses of 'popping rock' implications for primordial noble gases in the Earth, Science 276 (1997) 568–571.
[34] D.B. Patterson, M. Honda, I. McDougall, Atmospheric contamination: a possible source for heavy noble gases in basalts from Loihi Seamount, Hawaii, Geophys. Res. Lett. 17 (1990) 705–708.
[35] C.J. Ballentine, D.N. Barfod, The origin of air-like noble gases in MORB and OIB, Earth Planet. Sci. Lett. 180 (2000) 39–48.
[36] M. Moreira, J. Kunz, C. Allègre, Rare gas systematics in popping rock isotopic and elemental compositions in the upper mantle, Science 279 (1998) 1178–1181.
[37] K.A. Farley, H. Craig, Atmospheric argon contamination of ocean island basalt olivine phenocrysts, Geochim. Cosmochim. Acta 58 (1994) 2509–2517.

[38] M. Trieloff, J. Kunz, D.A. Clague, D. Harrison, C.J. Allègre, The nature of pristine noble gases mantle plumes, Science 288 (2000) 1036–1038.
[39] K.A. Farley, R.J. Poreda, Mantle neon and atmospheric contamination, Earth Planet. Sci. Lett. 114 (1993) 325–339.
[40] G. Turner, P. Burnard, D. Harrison, The plane truth about primordial noble gases in the Earth, in: 61st Meteoritical Society Meeting 33 (1998) A156–A157, Meteoritics, Dublin, Ireland.
[41] D.W. Harrison, P.G. Burnard, G. Turner, Noble gas behavior and composition in the Mantle: Constraints from the Iceland Plume, Earth Planet. Sci. Lett. 171 (1999) 199–207.
[42] D.R. Hilton, G.M. McMurtry, F. Goff, Large variations in vent fluid $CO_2/^3He$ ratios signal rapid changes in magma chemistry at Loihi Seamount, Hawaii, Nature 396 (1998) 359–362.
[43] B. Marty, A. Jambon, C/3He in volatile fluxes from the solid Earth: implications for carbon geodynamics, Earth Planet. Sci. Lett. 83 (1987) 16–26.
[44] B. Marty, L. Zimmerman, Volatiles (He, C, N, Ar) in mid-ocean ridge basalts: Assessment of shallow level fractionation and characterization of source composition, Geochim. Cosmochim. Acta 63 (1999) 3619–3633.
[45] J.E. Dixon, E. Stolper, An experimental study of water and carbon dioxide solubilities in mid-ocean ridge basaltic liquids. Part II: Applications to degassing, Contrib. Mineral. Petrol. 36 (1995) 1633–1646.
[46] Y. Nishio, S. Sasaki, T. Gamo, H. Hiyagon, Y. Sano, Carbon and helium isotope systematics of North Fiji Basin basalt glasses; carbon geochemical cycle in the subduction zone, Earth Planet. Sci. Lett. 154 (1998) 127–138.
[47] J.R. Holloway, Graphite-melt equilibria during mantle melting; constraints on CO2 in MORB magmas and the carbon content of the mantle, Chem. Geol. 147 (1998) 89–97.
[48] P. Burnard, Correction for volatile fractionation in ascending magmas: Noble gas abundances in primary mantle melts, Geochim. Cosmochim. Acta 65 (2001) 2605–2614.
[49] P.M. Nuccio, A. Paonita, Investigation of the noble gas solubility in H2O-CO2 bearing silicate liquids at moderate pressure; II, The extended ionic porosity (EIP) model, Earth Planet. Sci. Lett. 183 (2000) 499–512.
[50] M. Moreira, P. Sarda, Noble gas constraints on degassing processes, Earth Planet. Sci. Lett. 176 (2000) 375–386.
[51] H. Craig, W.B. Clark, M.A. Beg, Excess 3He in deep seawater on the East Pacific Rise, Earth Planet. Sci. Lett. 26 (1975) 125–132.
[52] K.A. Farley, E. Maier-Reimer, P. Schlosser, W. Broecker, Constraints on mantle 3He fluxes and deep-sea circulation from and oceanic general circulation model, J. Geophys. Res. 100 (B3) (1995) 3829–3839.
[53] P. Jean-Baptiste, Helium-3 distribution in the deep world ocean, in: Isotopes of Noble Gases as Tracers in Environmental Studies, Proc. IAEA (1992) 219–240.
[54] P.H. Sarda, D. Graham, Mid-ocean ridge popping rocks: implications for degassing at ridge crests, Earth Planet. Sci. Lett. 97 (1990) 268–289.
[55] D.E. Fisher, Helium, argon, and xenon in crushed and melted MORB, Geochim. Cosmochim. Acta 61 (1997) 3003–3012.
[56] J.E. Dixon, E. Stolper, J.R. Delaney, Infrared spectroscopic measurements of CO_2 and H_2O in Juan de Fuca Ridge basaltic glasses, Earth Planet. Sci. Lett. 90 (1988) 87–104.
[57] J.M. Sinton, R.S. Detrick, Mid-ocean ridge magma chambers, J. Geophys. Res. 97 (1992) 197–216.
[58] D.E. Fisher, M.R. Perfit, Evidence from rare gases for magma-chamber degassing of highly evolved mid-ocean-ridge basalt, Nature 343 (1990) 450–452.
[59] B. Marty, S. Zashu, M. Ozima, Two noble gas components in a Mid-Atlantic Ridge basalt, Nature 302 (1983) 238–240.
[60] P.J. Michael, W.C. Cornell, Influence of spreading rate and magma supply on crystallization and assimilation beneath mid-ocean ridges; evidence from chlorine and major element chemistry of mid-ocean ridge basalts, J. Geophys. Res. 103 (1998) 18325–18356.
[61] J.-i. Matsuda, B. Marty, The 40Ar/36Ar ratio of the undepleted mantle; a reevaluation, Geophys. Res. Lett. 22 (1995) 1937–1940.
[62] D.L. Anderson, The helium paradoxes, Proc. Natl. Acac. Sci. USA 95 (1998) 4822–4827.
[63] M. Honda, D.B. Patterson, Systematic elemental fractionation of mantle-derived helium, neon, and argon in mid-oceanic ridge glasses, Geochim. Cosmochim. Acta 63 (1999) 2863–2874.
[64] M.D. Kurz, W.J. Jenkins, J.-G. Schilling, S.R. Hart, Helium isotopic variations in the mantle beneath the central North Atlantic Ocean, Earth Planet. Sci. Lett. 58 (1982) 1–14.
[65] K.A. Farley, J. Natland, H. Craig, Binary mixing of enriched and undegassed (primitive?) mantle components (He, Sr, Nd, Pb) in Samoan lavas, Earth Planet. Sci. Lett. 111 (1992) 183–199.
[66] M. Condomines, K. Gronvold, P.J. Hooker, K. Muehlenbachs, R.K. O'Nions, N. Oskarsson, E.R. Oxburgh, Helium, oxygen, strontium and neodymium isotopic relationships in Icelandic volcanics, Earth Planet. Sci. Lett. 66 (1983) 125–136.
[67] D.R. Hilton, M.F. Thirlwall, R.N. Taylor, B.J. Murton, A. Nichols, Controls on magmatic degassing along the Reykjanes Ridge with implications for the helium paradox, Earth Planet. Sci. Lett. 183 (2000) 43–50.
[68] N. Jendrzejewski, T.W. Trull, F. Pineau, M. Javoy, Carbon solubility in mid-ocean ridge basaltic melt at low pressures (250–1950 bar), Chem. Geol. 138 (1997) 81–92.

Table 2. Abundances of He, Ne and CO_2 obtained by sequential crushing of Amsterdam – St. Paul basaltic glasses.

Sample	^{4}He x10^{-9}	^{20}Ne x10^{-12}	^{40}Ar x10^{-9}	^{40}Ar* x10^{-9}	CO_2 x10^{-3}
D76-2	38 ± 1	b.d.	1.62 ± 0.02	1.5 ± 1.4	0.35 ± 0.03
D76-2	972 ± 28	b.d.	37.1 ± 0.4	34.3 ± 6.2	6.06 ± 0.06
D76-2	1212 ± 35	b.d.	n.d.	n.d.	7.56 ± 0.07
D76-2	894 ± 26	21.7 ± 0.6	47.0 ± 0.4	31.4 ± 0.8	4.99 ± 0.05
D76-2	1041 ± 30	b.d.	34.6 ± 0.3	31.1 ± 4.1	2.3 ± 0.1
D76-2	**4157 ± 48**	**22 L.L.**	**119 L.L.**	**141 L.L.**	**21.3 ± 0.2**
D77-2	1084 ± 42	113 ± 8	139 ± 5	95 ± 5	9.07 ± 0.07
D77-2	3282 ± 128	72 ± 5	307 ± 10	283 ± 11	26.6 ± 0.2
D77-2	1691 ± 66	21 ± 2	145 ± 5	139 ± 5	10.8 ± 0.2
D77-2	423 ± 19	6.6 ± 0.8	38 ± 1	36 ± 1	<3
D77-2	**6480 ± 151**	**213 ± 10**	**629 ± 13**	**553 ± 13**	**46.5 L.L.**
D75-1	102 ± 3	b.d.	24.1 ± 0.2	20.0 ± 1.8	<3
D75-1	1253 ± 42	111 ± 2	277 ± 3	239 ± 3	20.6 ± 0.2
D75-1	1655 ± 117	92.9 ± 0.0	337 ± 3	326 ± 61	43.1 ± 0.3
D75-1	803 ± 27	13.9 ± 0.3	140 ± 1	136 ± 12	6.5 ± 0.1
D75-1	**3813 ± 127**	**218 L.L.**	**754 ± 4**	**721 ± 63**	**70.2 L.L.**
WC49	104 ± 1	12.8 ± 1.4	26 ± 1	22 ± 1	<3
WC49	996 ± 10	36 ± 2	201 ± 5	186 ± 5	16.0 ± 0.2
WC49	842 ± 9	23 ± 2	162 ± 3	152 ± 3	11.3 ± 0.2
WC49	711 ± 7	20 ± 2	136 ± 3	128 ± 3	9.50 ± 0.09
WC49	551 ± 6	17.9 ± 1.5	104 ± 2	94 ± 2	5.3 ± 0.2
WC49	**3204 ± 16**	**110 ± 4**	**629 ± 7**	**583 ± 7**	**42.0 L.L.**
WC47	45 ± 0	5.5 ± 0.8	1.6 ± 0.1	0.6 ± 0.1	<3
WC47	645 ± 6	53 ± 3	38 ± 1	13 ± 1	23.5 ± 0.2
WC47	803 ± 8	9.0 ± 0.9	12.9 ± 0.3	9.7 ± 0.3	22.0 ± 0.2
WC47	508 ± 5	178 ± 6	109 ± 2	23 ± 2	10.9 ± 0.2
WC47	**2001 ± 11**	**245 ± 7**	**161 ± 2**	**46 ± 2**	**56.4 L.L.**
D73-3	140 ± 4	24 ± 1	29 ± 1	12 ± 1	<3
D73-3	907 ± 24	59 ± 3	96 ± 3	74 ± 3	15.9 ± 0.1
D73-3	1236 ± 33	240 ± 10	263 ± 8	131 ± 8	19.1 ± 0.2
D73-3	327 ± 9	358 ± 15	67 ± 2	17 ± 2	<3
D73-3	**2610 ± 41**	**682 ± 19**	**454 ± 9**	**233 ± 9**	**35.0 L.L.**
D73-4	32 ± 1	14.3 ± 0.8	21.4 ± 0.4	16.4 ± 0.4	0.40 ± 0.05
D73-4	799 ± 13	60 ± 3	273 ± 5	246 ± 5	7.64 ± 0.08
D73-4	371 ± 6	18.1 ± 1.0	184 ± 4	176 ± 4	<3
D73-4	**1201 ± 14**	**93 ± 4**	**478 ± 6**	**439 ± 6**	**8.0 L.L.**
D73-5	17 ± 1	1.4 ± 0.0	10.1 ± 0.1	7.4 ± 0.1	<3
D73-5	997 ± 46	105 ± 4	1983 ± 24	1869 ± 24	7.26 ± 0.07
D73-5	**1013 ± 46**	**107 ± 4**	**1993 ± 24**	**1876 ± 24**	**7.26 L.L.**
WC46	676 ± 9	19.4 ± 1.3	105 ± 4	98 ± 4	13.3 ± 0.3
WC46	738 ± 10	12.8 ± 1.0	109 ± 4	104 ± 4	14.5 ± 0.2
WC46	667 ± 9	22.7 ± 1.4	100 ± 3	90 ± 3	11.2 ± 0.2
WC46	138 ± 2	4.7 ± 0.9	15 ± 1	13 ± 1	<3
WC46	**2218 ± 17**	**60 ± 2**	**328 ± 6065 1**	**305 ± 6**	**39.0 L.L.**
D71-3	17 ± 0	14.7 ± 0.5	8.0 ± 0.1	0.4 ± lim	<3
D71-3	119 ± 3	27.1 ± 0.7	11.6 ± 0.1	0.5 ± 0.0	<3

Table 2 (cont)

D71-3	204 ± 6	28.4 ± 0.8	16.3 ± 0.2	1.6 ± 0.0	2.74 ± 0.05
D71-3	219 ± 6	24.5 ± 0.5	7.8 ± 0.1	0.4 ± 0.0	<3
D71-3	**559 ± 9**	**95 ± 1**	**35.7 ± 0.2**	**1.6 ± lim**	**2.74 L.L.**
D71-1	7 ± 0	5.4 ± 0.4	1.3 ± 0.1	0.9 ± 0.1	<3 ± 0.04
D71-1	108 ± 2	7.0 ± 0.4	2.9 ± 0.1	1.4 ± 0.1	<3 ± 0.03
D71-1	126 ± 2	23.7 ± 1.2	9.6 ± 0.2	0.5 ± lim	<3 ± 0.05
D71-1	**241 ± 3**	**36.2 ± 1.3**	**13.8 ± 0.2**	**2.8 ± lim**	**0.00 L.L.**
D64-2	27 ± 1	1.4 ± 0.1	5.2 ± 0.1	0.2 ± 0.1	<3
D64-2	465 ± 22	23.6 ± 0.8	33.2 ± 0.4	2.9 ± 0.4	7.38 ± 0.07
D64-3	**492 ± 22**	**25.0 ± 0.8**	**38.4 ± 0.4**	**3.1 ± 0.4**	**7.38 L.L.**
D63-1	26.32 ± 0.44	b.d. ±	0.90 ± 0.04	0.0 ± lim	<3
D63-1	944 ± 16	760 ± 18	304 ± 9	14 ± lim	18.2 ± 0.2
D63-1	329 ± 5	183 ± 4	16.5 ± 0.5	0.8 ± lim	3.0 ± 0.2
D63-1	**1300 ± 17**	**943 L.L.**	**321 ± 9**	**15 ± lim**	**21.2 ± L.L.**
D60-1	122 ± 2	20 ± 2	22 ± 1	7 ± 1	<3
D60-1	354 ± 5	155 ± 8	91 ± 3	21 ± 3	6.11 ± 0.07
D60-1	661 ± 9	277 ± 20	168 ± 6	22 ± 6	9.9 ± 0.2
D60-1	311 ± 4	186 ± 10	98 ± 3	17 ± 3	3.7 ± 0.3
D60-1	**1448 ± 11**	**638 ± 24**	**379 ± 8**	**67 ± 8**	**19.6 L.L.**
D47-6	504 ± 17	175 ± 2	154 ± 2	72 ± 1	7.85 ± 0.06
D47-6	391 ± 13	b.d.	72 ± 1	49 ± 1	5.72 ± 0.05
D47-6	815 ± 27	137 ± 2	161 ± 2	95 ± 1	10.2 ± 0.1
D47-6	310 ± 9	b.d.	163 ± 2	40.2 ± 0.4	3.86 ± 0.09
D47-6	373 ± 11	b.d.	129 ± 1	48 ± 1	<3
D47-6	**2392 ± 37**	**312 L.L.**	**680 ± 3**	**304 ± 2**	**27.6 L.L.**
D43-2	71 ± 2	b.d.	20.9 ± 0.2	16.1 ± 1.1	<3
D43-2	510 ± 15	33.9 ± 0.8	110 ± 11	93 ± 13	<3
D43-2	23 ± 1	b.d.	6.1 ± 0.1	4.8 ± 1.0	<3
D43-2	**604 ± 40**	**34 L.L.**	**137 ± 78**	**113 ± 13**	**b.d.**
D39-1	26 ± 1	13 ± 2	10 ± 1	1 ± 1	<3
D39-1	545 ± 21	23 ± 2	38 ± 1	32 ± 1	<3
D39-1	1099 ± 43	234 ± 16	178 ± 6	69 ± 6	7.2 ± 0.3
D39-1	811 ± 32	47 ± 3	55 ± 2	44 ± 2	12.3 ± 0.5
D39-1	**2481 ± 57**	**317 ± 17**	**281 ± 6**	**146 ± 6**	**19.6 L.L.**
D34-1	144 ± 6	4.1 ± 0.5	2.2 ± 0.5	1.9 ± 0.5	<3
D34-1	1312 ± 52	15 ± 2	21 ± 1	17 ± 1	9.22 ± 0.07
D34-1	1081 ± 43	14.8 ± 1.1	21 ± 1	16 ± 1	6.93 ± 0.06
D34-1	164 ± 6	10.3 ± 1.2	7 ± 1	2 ± 1	<3
D34-1	**2702 ± 67**	**45 ± 2**	**51 ± 1**	**37 ± 1**	**16.1 L.L.**
D33-1	501 ± 8	6.9 ± 0.2	18 ± 2	16 ± lim	3.67 ± 0.03
D33-1	3125 ± 51	58 ± 2	129 ± 11	104 ± 11	23.4 ± 0.2
D33-1	2259 ± 37	22.5 ± 0.7	145 ± 13	129 ± 13	14.5 ± 0.1
D33-1	2120 ± 34	41.4 ± 1.2	74 ± 7	66 ± 7	9.2 ± 0.2
D33-1	**8004 ± 72**	**129 ± 2**	**367 ± 18**	**316 ± L.L.**	**50.8 ± 0.3**

All units are cm^3 STP released.
L.L. = Lower Limit

Table 3. Isotopic compostion of He, Ne, and Ar trapped in basaltic glasses from the Amsterdam – St. Paul platform

Sample	$^{3}He/^{4}He$	$^{21}Ne/^{22}Ne$	$^{20}Ne/^{22}Ne$	$^{40}Ar/^{36}Ar$	Comments
D76-2	9.0 ± 0.5	b.d.	b.d.	2959 ± 2868	
D76-2	8.1 ± 0.4	b.d.	b.d.	3844 ± 690	
D76-2	n.d.	b.d.	b.d.		
D76-2	8.0 ± 0.4	0.041 ± 0.001	13.0 ± 0.3	890 ± 21	
D76-2	8.0 ± 0.4	b.d.	b.d.	2933 386	
D76-2	**8.1 ± 0.1**				
D77-2	8.8 ± 0.2	0.032 ± 0.002	10.4 ± 0.9	910 ± 51	
D77-2	9.1 ± 0.1	0.036 ± 0.003	11.3 ± 1.0	3068 ± 177	
D77-2	8.8 ± 0.1	0.037 ± 0.004	10.8 ± 0.9	6932 ± 608	
D77-2	n.d. ± 0.9	b.d.	b.d.	7992 ± 2439	
D77-2	**8.4 ± 0.2**				**minor plag**
D75-1	9.2 ± 0.5	b.d.	b.d.	1767 ± 159	
D75-1	8.7 ± 0.5	0.033 ± 0.001	10.7 ± 0.2	2145 ± 22	
D75-1	8.5 ± 0.9	0.038 ± 0.001	11.1 ± 0.2	9408 ± 1767	
D75-1	8.7 ± 0.5	b.d.	b.d.	10216 ± 934	
D75-1	**8.7 ± 0.3**				
WC49	12.8 ± 0.3	b.d.	b.d.	1929 ± 267	
WC49	10.5 ± 0.2	0.037 ± 0.003	11.1 ± 0.6	3977 ± 473	
WC49	11.0 ± 0.2	0.038 ± 0.004	11.1 ± 0.8	4955 ± 603	
WC49	11.3 ± 0.3	b.d.	b.d.	4892 ± 606	
WC49	12.0 ± 0.3	b.d.	b.d.	3286 ± 399	
WC49	**11.1 ± 0.1**				
WC47	15.8 ± 0.5	b.d.	b.d.	488 ± 95	
WC47	16.4 ± 0.3	0.031 ± 0.002	10.4 ± 0.5	449 ± 43	
WC47	15.9 ± 0.3	b.d.	b.d.	1180 ± 143	
WC47	16.2 ± 0.3	0.030 ± 0.002	9.9 ± 0.4	375 ± 35	
WC47	**16.1 ± 0.1**				
D73-3	13.3 ± 0.5	0.028 ± 0.002	8.7 ± 0.2	509 ± 52	
D73-3	14.7 ± 0.3	0.034 ± 0.002	10.8 ± 0.2	1247 ± 125	
D73-3	14.2 ± 0.2	0.030 ± 0.001	10.1 ± 0.2	588 ± 58	
D73-3	14.6 ± 0.6	0.031 ± 0.001	10.6 ± 0.2	395 ± 39	
D73-3	**14.4 ± 0.4**				
D73-4	10.7 ± 0.5	b.d.	b.d.	1276 ± 238	
D73-4	11.4 ± 0.3	0.035 ± 0.003	10.8 ± 0.7	3039 ± 483	
D73-4	12.0 ± 0.3	b.d.	b.d.	7185 ± 1237	
D73-4	**11.5 ± 0.2**				**plag**
D73-5	12.3 ± 0.7	b.d.	b.d.	1083 ± 183	
D73-5	11.8 ± 0.2	0.031 ± 0.001	9.6 ± 0.3	5145 ± 105	
D73-5	**11.9 ± 0.8**				**plag**
WC46	14.2 ± 0.3	b.d.	b.d.	4435 ± 775	
WC46	14.6 ± 0.4	b.d.	b.d.	7280 ± 1371	
WC46	13.9 ± 0.1	0.030 ± 0.002	9.7 ± 0.6	2927 ± 493	
WC46	14.4 ± 0.2	b.d.	b.d.	3602 ± 958	
WC46	**14.2 ± 0.1**				**minor plag**
D71-3	10.8 ± 0.8	b.d.	b.d.	265 ± 17	
D71-3	9.7 ± 0.5	0.030 ± 0.001	10.2 ± 0.2	309 ± 18	

Table 3 (cont)

D71-3	9.6 ± 0.5	0.031 ± 0.001	10.3 ± 0.2	329 ± 8	
D71-3	9.4 ± 0.5	0.032 ± 0.001	10.2 ± 0.2	310 ± 20	
D71-3	**9.6 ± 0.3**				**plag**
D71-1	9.0 ± 1.5	b.d.	b.d.	962 ± 1157	
D71-1	10.0 ± 0.3	b.d.	b.d.	589 ± 243	
D71-1	10.9 ± 0.3	0.031 ± 0.003	10.1 ± 0.6	280 ± 46	
D71-1	**10.4 ± 0.3**				**minor plag**
D64-2	10.1 ± 0.5	b.d.	b.d.	309 ± 22	
D64-2	10.6 ± 0.4	0.030 ± 0.001	10.2 ± 0.2	324 ± 5	
D64-3	**10.6 ± 0.7**				
D63-1	11.4 ± 0.4	b.d.	b.d.	249 ± 18	
D63-1	12.0 ± 0.2	0.030 ± 0.001	9.5 ± 0.1	284 ± 12	
D63-1	12.8 ± 0.1	0.030 ± 0.001	9.8 ± 0.2	309 ± 14	
D63-1	**12.2 ± 0.3**				**brown alteration**
D60-1	11.6 ± 0.3	b.d.	b.d.	436 ± 73	
D60-1	11.5 ± 0.5	0.029 ± 0.002	9.9 ± 0.5	382 ± 61	
D60-1	11.3 ± 0.3	0.028 ± 0.002	10.1 ± 0.7	340 ± 53	
D60-1	10.9 ± 0.3	0.029 ± 0.002	10.0 ± 0.5	358 ± 56	
D60-1	**11.3 ± 0.1**				**minor plag**
D47-6	9.6 ± 1.0	0.030 ± 0.001	10.2 ± 0.2	550 ± 3	
D47-6	7.7 ± 0.6	b.d.	b.d.	946 ± 14	
D47-6	7.6 ± 0.4	0.031 ± 0.001	10.5 ± 0.2	717 ± 4	
D47-6	8.0 ± 0.4	b.d.	b.d.	392 ± 1	
D47-6	7.8 ± 0.4	b.d.	b.d.	471 ± 2	
D47-6	**8.1 ± 0.2**				**minor plag**
D43-2	8.1 ± 0.5	b.d.	b.d.	1284 ± 85	
D43-2	7.8 ± 0.4	0.035 ± 0.001	11.0 ± 0.2	1845 ± 186	
D43-2	8.6 ± 0.6	b.d.	b.d.	1392 ± 298	
D43-2	**7.8 ± 0.7**				
D39-1	8.1 ± 0.4	b.d.	b.d.	341 ± 29	
D39-1	7.8 ± 0.1	0.035 ± 0.002	13.3 ± 0.7	1731 ± 151	
D39-1	8.3 ± 0.2	0.029 ± 0.001	10.0 ± 0.7	477 ± 26	
D39-1	7.5 ± 0.1	0.032 ± 0.002	10.4 ± 0.4	1453 ± 99	
D39-1	**7.9 ± 0.2**				**minor plag**
D34-1	9.3 ± 0.1	b.d.	b.d.	2020 ± 2984	
D34-1	9.3 ± 0.1	b.d.	b.d.	1610 ± 219	
D34-1	9.0 ± 0.1	b.d.	b.d.	1287 ± 149	
D34-1	9.3 ± 0.1	b.d.	b.d.	451 ± 59	
D34-1	**9.2 ± 0.2**				
D33-1	9.9 ± 0.3	b.d.	b.d.	3598 lim	
D33-1	10.0 ± 0.1	0.035 ± 0.002	10.5 ± 0.2	1493 ± 154	
D33-1	9.9 ± 0.1	0.044 ± 0.003	11.7 ± 0.3	2674 ± 331	
D33-1	9.8 ± 0.1	0.036 ± 0.002	10.7 ± 0.2	2777 ± 275	
D33-1	**9.9 ± 0.1**				**minor plag**

$^{40}Ar/^{36}Ar$ and $^{20}Ne/^{22}Ne$ ratios not reported for the sample totals as the air contamination in early crush steps biases these values: the maximum ratios measured are more representative of the trapped gases.